INTRODUCTION

The loss of myocytes as a consequence of AMI (acute myocardial infarction) results in progressive changes in ventricular architecture [1,2]. This process, defined as post-infarction ventricular remodelling, is associated with a higher mortality and a higher incidence of complications, such as the development of heart failure, aneurysm formation and ventricular rupture [3,4]. During the remodelling process, as well as intrinsic changes in cardiac myocytes, it has been recognized that important alterations also occur within the extracellular matrix of the myocardium [5,6].

MMPs (matrix metalloproteinases) belong to a family of zinc-containing endoproteinases responsible for extracellular protein degradation, and are inhibited by specific tissue inhibitors [TIMP (tissue inhibitor of metalloproteinases)] [5,6]. In experimental myocardial infarction, MMPs are up-regulated in myocardial tissues, and are the driving force in extracellular matrix remodelling and infarct expansion [7,8]. Among the MMPs, the importance of MMP-9 during the processes of infarct healing and LV (left ventricular) remodelling has been demonstrated in previous studies using genetically modified mice [9,10]. Infarcted mice with the targeted deletion of MMP-9 had a decreased incidence of early myocardial rupture [9] and progressive LV dilation [10]. However, in the clinical setting, there has been little evidence regarding the production of MMPs in the infarcted human heart.

Statins have various cardiovascular protective actions, including anti-inflammatory and anti-apoptotic actions, independent of their effects on cholesterol levels. A study using a mouse AMI model demonstrated that statin treatment attenuated LV remodelling [11], which was associated with decreased MMP activity [12].

In the present study, we hypothesized that cardiac MMP activation may be associated with the degree of LV enlargement and the level of BNP (brain natriuretic peptide), a biochemical marker of post-infarction remodelling [13,14]. If so, MMP production may be attenuated by statin treatment in patients with AMI.

MATERIALS AND METHODS

Patients

This study included 30 male patients. All of the patients gave their written informed consent prior to participation in the study. The Institutional Ethical Committee on Human Research approved the study protocol. Patients with the following disorders were excluded from the study: prior myocardial infarction, and liver (elevated activities of aminotransferases), kidney (elevated level of creatinine or urea) or lung dysfunction (restrictive or obstructive pattern in spirometry).

The control group consisted of ten patients with stable AP (angina pectoris), who complained of symptoms consistent with Canadian Cardiovascular Society Classification of angina level I, II or III, with evidence of myocardial ischaemia. All of the control patients had no evidence of a previous AMI, and had severe coronary artery stenosis and therefore underwent coronary angioplasty (with adjunctive stenting in five patients). The treated sites were the left anterior descending artery in four patients (40 %), the right or left circumflex artery in four patients (40 %), and both the left anterior descending and right coronary arteries in two patients (20 %).

We also studied 20 patients with AMI who fulfilled the following criteria: typical chest pain > 30 min of duration, ST segment elevation > 0.1 mV in two or more ECG leads with the subsequent evolution of a typical infarct pattern, and increased serum CK (creatine kinase) level. A total of 14 patients underwent PTCA (percutaneous transluminal coronary angioplasty) of the infarct-related artery (with adjunctive stenting in nine patients), and the remaining six patients received an intravenous administration of a tissue-type plasminogen activator and/or heparin in the acute phase. In all the patients, coronary angiography immediately after treatment showed a TIMI 3 grade flow in the infarct-related artery. The elapsed time to reperfusion was 4.6 h on average. The infarct sites were in the anterior wall in ten patients (50 %), the inferior wall in seven patients (35 %) and the postero-lateral wall in three patients (15 %). In this study, all of the patients with AMI were treated with the ACE-I (angiotension-converting enzyme inhibitor) enalapril (5 mg) after their hospital admission. Among them, ten patients with hyperlipidaemia (total cholesterol level > 220 mg/dl) were treated with 10 mg of pravastatin; the remaining ten patients did not have hyperlipidaemia and thus did not receive pravastatin. A recent Management of Elevated Cholesterol in the Primary Prevention Group of Adult Japanese (MEGA) trial [14a] has shown a similar decrease in coronary artery disease incidence following treatment with 10–20 mg of pravastatin used in Asia to that observed for 20–40 mg doses used in Europe and the United States.

Cardiac catheterization and analysis of LV function

In patients with AMI, chronic-stage cardiac catheterization was repeated approx. 3–4 weeks after the onset of AMI. A 5 French multipurpose catheter (Cathex) was introduced into the CS (coronary sinus) through the left subclavian vein under fluoroscopic guidance [14]. The position of the catheter tip was confirmed by the injection of contrast medium. Blood samples were collected from the CS before the intravenous administration of heparin. Following the collection of blood samples from the right brachial artery (as peripheral blood samples) through a 6 French sheath, heparin was administered and coronary

angiography and left ventriculography were performed, according to the conventional Judkins' technique. LV pressure was measured using a 2 French high-fidelity micromanometer catheter (Miller Instruments) advanced into the left ventricle via the lumen of a 6 French pig-tail catheter. The restenosis of a treated artery was defined as an arterial narrowing of >75%, as determined by coronary angiography.

LV volume was evaluated angiographically by a cardiologist who was blinded to the results of the biochemical assays. Ventricular silhouettes in a 30° right anterior oblique projection were digitized using an ANCHOR ventriculography analysis system (Siemens-Elema). Using the area-length method, LV end-systolic volume index, LVEDVI (LV end-diastolic volume index) and LVEF (LV ejection fraction) were calculated.

Biochemical assessment

Blood samples were centrifuged and serum was stored at −80 °C until assay. A sandwich enzyme immunoassay was performed to determine MMP-2 level (Fuji Chemical Industries) [15]. In addition, the level of MMP-9, another gelatinase-like MMP-2, and that of MMP-13, an interstitial collagenase, were analysed using MMP Biotrak enzyme-linked immunoadsorbent assay kits (Amersham Biosciences). The levels were back-calculated from the standard curve determined with the enzyme-linked immunoadsorbent assay kits using a 96-well microplate reader (Emax; Molecular Devices). These kits detect the pro-enzyme and the pro-enzyme complexed with TIMP. The detection limits were 0.5 ng/ml for MMP-2, 0.6 ng/ml for MMP-9 and 0.03 ng/ml for MMP-13.

We also measured levels of TIMP-1 (Fuji Chemical Industries) and TIMP-2 (Amersham Biosciences) using sandwich enzyme immunoassays [15]. The detection limits for TIMP-1 and TIMP-2 were 1.2 and 8.0 ng/ml respectively.

BNP was measured using specific immunoradiometric assay kits (Shionogi). The sensitivity of these kits was 2 pg/ml. Ang II (angiotensin II) and TGF-β (transforming growth factor-β) levels were also measured, as reported previously [16].

The serum CRP (C-reactive protein) level was measured by N Latex CRP II monoassay using a nephelometric analyser (BN II; Dade Behring). The lower detection limit of this test was 0.06 mg/dl. Total cholesterol, triacylglycerol (triglyceride) and HDL (high-density lipoprotein) cholesterol concentrations were determined by enzymatic methods using a Toshiba TBA 80M analyser. LDL (low-density lipoprotein) was calculated using Fredewald's formula. We also measured WBC (white blood cell) number.

Statistical analysis

The two groups were compared by Student's t test. Measurements from the CS and the peripheral artery were compared within a group by ANOVA. When a significant difference among groups was indicated by the initial analysis, individual paired comparisons were determined using the Student–Newman–Keuls method. A linear regression line was calculated by the least-square method to assess the correlation between two parameters. To investigate independent predictors, we used multivariate logistic regression analysis. In all cases, differences were considered significant at $P < 0.05$. Results are presented as means ± S.D., or medians.

Table 1 Clinical characteristics

*$P = 0.05$ and **$P < 0.01$ compared with control (patients with stable AP).

Characteristic	Patients with AMI ($n = 20$)	Patients with stable AP ($n = 10$)
Age (years)	66 ± 9	67 ± 6
Peak CK (units/l)	1986 (801–8574)	–
Cardiac function		
LVEF (%)	48 ± 7**	58 ± 7
LVEDVI (ml/m^2)	95 ± 18**	55 ± 21
Vessels >75% stenosed (n)	1.5 ± 0.7	1.6 ± 0.7
Risk factors (n)		
Hypertension	11 (55%)	7 (70%)
Diabetes mellitus	15 (75%)	6 (60%)
Hyperlipidaemia	10 (50%)	6 (60%)
Smoking	12 (60%)	6 (60%)
Biochemical parameters†		
Total cholesterol (mg/dl)	193 ± 27	198 ± 20
LDL (mg/dl)	120 ± 30	122 ± 31
WBC count (cells/μl)	6615 ± 1571	5600 ± 1063
CRP (mg/dl)	0.34 ± 0.33*	0.13 ± 0.06
Medication used (n)		
ACE-I	20 (100%)	4 (40%)
β-Blockers	11 (55%)	6 (60%)
Statins	10 (50%)	6 (60%)
Calcium antagonists	7 (35%)	5 (50%)
Nitrates	4 (20%)	2 (20%)
Aspirin	20 (100%)	10 (100%)

† Data obtained on the day when cardiac catheterization was performed.

RESULTS

The baseline clinical characteristics of the patients with AMI and the control patients with AP (without evidence of AMI) are summarized in Table 1. In the patients with AMI, cardiac function data were obtained at chronic-stage cardiac catheterization performed 22 ± 12 days after the onset of AMI. Coronary angiography revealed 90% stenosis of the infarct-related artery in two patients and 100% stenosis in three patients. These five patients with restenosis had received intravenous thrombolysis alone in the acute stage. In the remaining 15 patients, the treated

Table 2 Comparisons of BNP, MMP and TIMP levels in the CS and peripheral artery

*$P < 0.05$ compared with levels in artery; †$P < 0.05$ compared with control (patients with stable AP).

	Patients with AMI ($n = 20$)		Patients with stable AP ($n = 10$)	
Peptide	CS	Artery	CS	Artery
BNP (pg/ml)	400 ± 376*†	126 ± 176	54 ± 25	52 ± 25
MMP-2 (ng/ml)	853 ± 199*†	716 ± 127	631 ± 44	630 ± 46
MMP-9 (ng/ml)	165 ± 129*†	98 ± 82	68 ± 25	71 ± 24
MMP-13 (ng/ml)	0.05 ± 0.04	0.05 ± 0.02	0.04 ± 0.02	0.04 ± 0.02
TIMP-1 (ng/ml)	155 ± 59	150 ± 53	130 ± 33	134 ± 32
TIMP-2 (ng/ml)	112 ± 18	108 ± 14	94 ± 11	97 ± 16

sites remained patent. With the exception of cardiac function (LVEF and LVEDVI) and the prevalence of ACE-I use, clinical characteristics were similar between patients with AMI and AP.

Enhancement of cardiac MMP production in patients with AMI

Table 2 shows the comparison of BNP, MMP and TIMP levels between blood samples from the CS and peripheral artery. In patients with AMI, levels of BNP, MMP-2 and MMP-9 were significantly ($P < 0.05$) higher in the CS than in the peripheral artery, whereas the levels of MMP-13, TIMP-1 and TIMP-2 were similar. In control patients with AP, no significant differences in the levels of BNP, MMPs and TIMPs were observed between the CS and peripheral artery. These findings indicate that the production of MMP-2 and MMP-9, as well as that of BNP, is enhanced in an infarcted heart.

Correlation of cardiac MMP production with post-infarction LV remodelling

In patients with AMI, the CS–arterial concentration gradients of MMP-2 and MMP-9 correlated positively with those of BNP and LVEDVI respectively (Figure 1), but not with LVEF, peak CK level and circulating WBC counts. These myocardial gradients were not different between patients with and without progression to restenosis (MMP-2, 87 ± 32 compared with 152 ± 173 ng/ml; MMP-9, 83 ± 86 compared with 61 ± 82 ng/ml).

Comparisons between pravastatin-treated patients with AMI and non-pravastatin-treated patients with AMI

We then compared levels of MMPs between ten patients treated with 10 mg of pravastatin and ten patients not treated with pravastatin (Table 3). Although the total cholesterol level before treatment was higher ($P < 0.05$) in the pravastatin-treated patients with AMI (223 ± 7 mg/dl in treated patients compared with 195 ± 17 mg/dl in

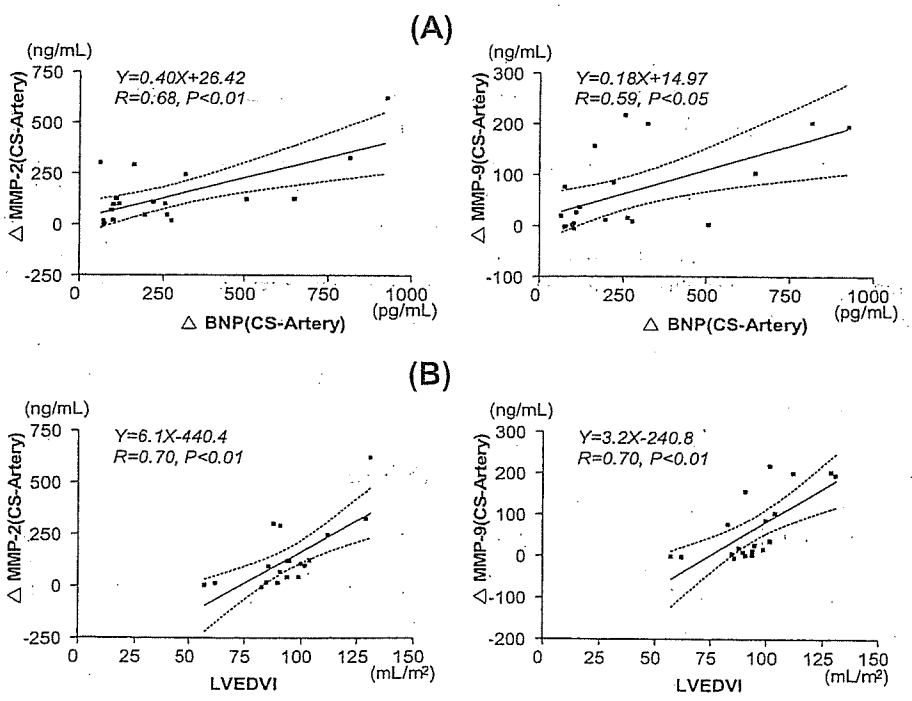

Figure 1 Correlations between CS–arterial concentration gradients of MMP-2 and -9 and BNP (A) and LVEDVI (B) in 20 patients with AMI

Table 3 Comparisons of MMPs between pravastatin-treated and non-pravastatin-treated patients

* $P < 0.05$ compared with levels in artery; † $P < 0.05$ compared with levels in non-pravastatin-treated patients. CS–artery, CS–arterial concentration gradient.

	Patients with AMI						Patients with stable AP					
	Pravastatin-treated ($n = 10$)			Non-pravastatin-treated ($n = 10$)			Pravastatin-treated ($n = 6$)			Non-pravastatin-treated ($n = 4$)		
MMP (ng/ml)	CS	Artery	CS–artery	CS	Artery	CS–artery	CS	Artery	CS–artery	CS	Artery	CS–artery
MMP-2	808 ± 182	739 ± 158	69 ± 43†	897 ± 216*	684 ± 84	213 ± 185	631 ± 53	624 ± 51	7 ± 23	629 ± 32	639 ± 43	−9 ± 53
MMP-9	94 ± 61†	80 ± 59	14 ± 27†	236 ± 142*	117 ± 100	119 ± 84	68 ± 20	72 ± 16	−4 ± 4	68 ± 20	69 ± 29	0 ± 5
MMP-13	0.06 ± 0.06	0.03 ± 0.03	0.03 ± 0.06	0.03 ± 0.02	0.05 ± 0.03	−0.01 ± 0.03	0.03 ± 0.04	0.04 ± 0.02	−0.01 ± 0.01	0.04 ± 0.02	0.03 ± 0.02	0.01 ± 0.03

non-treated patients), no significant differences were observed after treatment between the two groups (183 ± 31 mg/dl in treated patients compared with 201 ± 20 mg/dl in non-treated patients). Levels of CRP (0.18 ± 0.13 mg/dl in treated patients compared with 0.50 ± 0.40 mg/dl in non-treated patients; $P = 0.03$) and the CS–arterial concentration gradients of MMP-2 and MMP-9 (Table 3) were significantly different between the two groups. However, the concentration gradients of TGF-β and Ang-II were similar between patients treated with pravastatin and those not treated (Ang-II, 19.5 ± 20.2 compared with 36.9 ± 32.4 pg/ml respectively; TGF-β, 1.2 ± 3.3 compared with 2.1 ± 4.7 pg/ml respectively).

We then performed multivariate analysis for the predictors of CS–arterial concentration gradients of MMP levels, including age, sex, coronary risk factors, peak CK, infarct site (anterior wall), CRP, TIMP, pravastatin treatment, LVEF and LVEDVI. The association between pravastatin treatment and cardiac MMP-2 production was modest, with an odds ratio of 0.074 (95 % confidence interval, 0.005–1.109; $P = 0.06$), and did not reach statistical significance.

DISCUSSION

The major findings of the present clinical study are that after AMI, the cardiac production of MMP-2 and MMP-9 is enhanced and associated with LV enlargement and BNP secretion, and that the pleiotropic effect of statins appears to be associated with the modulation of cardiac MMP activation.

Among the MMP species, MMP-2 and MMP-9 play an important role in LV remodelling, as these MMPs are activated in the myocardium and it has been reported that the targeted deletion of these MMPs prevents post-infarction cardiac dysfunction and rupture [9,10]. In the clinical setting, circulating MMP-2 and MMP-9 levels have been measured in previous studies of patients with AMI [17–19]; however, these results were conflicting. Squire et al. [17] reported that circulating MMP levels were inversely correlated with LV dilatation, whereas Matsunage et al. [18] and Nakaya et al. [19] found that serum MMP levels and activity were positively correlated with LV dilatation. In addition, circulating MMP levels could be affected at the acute stage following reperfusion therapy and by the clinically vulnerable state [20–23]. In the present study, we focused on cardiac production of MMP [14], and the measurement was performed at the clinically stable stage following AMI. As shown in Table 2, despite similar levels of TIMPs, significant differences in levels of BNP, MMP-2 and MMP-9 were observed between the CS and the peripheral artery in patients with AMI. To our knowledge, this is the first study demonstrating the enhanced production of MMP-2 and MMP-9 in a human infarcted heart. Moreover, as shown

in Figure 1, the CS–arterial concentration gradients of MMP-2 and MMP-9 correlated positively with those of BNP and LVEDVI. Taking into account the delicate balance between MMPs and TIMPs in tissue remodelling, the present findings indicate that excessive cardiac production of MMPs may play an important pathological role in the progression of post-infarction LV dysfunction.

A previous experimental study of an AMI model using BNP-transgenic mice demonstrated a potential interaction of BNP with inflammation [24]. The overexpression of BNP leads to neutrophil infiltration and MMP-9 expression in the infarct region and increases the incidence of cardiac rupture. These findings suggest the significance of inflammatory reaction in the heart accompanied by changes in LV function. 3-Hydroxy-3-methylglutaryl-CoA reductase inhibitors, such as statins, exert various cardiovascular protective effects beyond their lipid-level lowering actions [12,25]. These pleiotropic effects include the inhibition of inflammatory responses. In the present study, we have shown that the CS–arterial concentration gradients of MMP-2 and MMP-9 were smaller in the pravastatin-treated group than in the non-pravastatin-treated group, which was accompanied by a decrease in CRP level. These findings indicate that pravastatin may modulate cardiac MMP production in patients with AMI, probably via its anti-inflammatory effects. Similar observations of decreased circulating MMP-2 levels in patients with AMI treated with 10 mg of paravastain have been reported previously [19].

There are several potential limitations of the present study. First, this study was not randomized. Pravastatin was administered to a small number of patients with AMI with hyperlipidaemia. In such a pro-inflammatory state, tissue MMPs might have been activated before treatment [26], which could affect the results. Therefore prospective studies will be required to determine if pravastatin has a causal role in reducing cardiac MMP production in patients with AMI. Secondly, the present study was carried out over the short term, whereas ventricular remodelling is known to progress over months or years. Thirdly, previous studies have shown that the renin–angiotensin system is also involved in the induction of post-infarction ventricular remodelling [27] and can be inhibited by statins [28,29]. However, we have shown that the CS–arterial concentration gradients of Ang II were similar between pravastatin-treated patients and non-pravastatin-treated patients. This may be related, in part, to the fact that all our patients with AMI had been treated with 5 mg of enalapril.

In conclusion, the present study demonstrates the enhancement of MMP production in an infarcted heart. Pleiotropic effects of statins may be associated with the modulation of cardiac MMP activation, which is potentially beneficial in the attenuation of post-infarction LV remodelling.

REFERENCES

1 Sutton, M. G. and Sharpe, N. (2000) Left ventricular remodeling after myocardial infarction: pathophysiology and therapy. Circulation 101, 2981–2988
2 Yousef, Z. R., Redwood, S. R. and Marber, M. S. (2000) Postinfarction left ventricular remodelling: where are the theories and trials leading us? Heart 83, 76–80
3 White, H. D., Norris, R. M., Brown, M. A., Brandt, P. W., Whitlock, R. M. and Wild, C. J. (1987) Left ventricular end-systolic volume as the major determinant of survival after recovery from myocardial infarction. Circulation 76, 44–51
4 Weisman, H. F. and Healy, B. (1987) Myocardial infarct expansion, infarct extension, and reinfarction: pathophysiologic concepts. Prog. Cardiovasc. Dis. 30, 73–110
5 Creemers, E. E., Cleutjens, J. P., Smits, J. F. and Daemen, M. J. (2001) Matrix metalloproteinase inhibition after myocardial infarction: a new approach to prevent heart failure? Circ. Res. 89, 201–210
6 Spinale, F. G. (2002) Matrix metalloproteinases: regulation and dysregulation in the failing heart. Circ. Res. 90, 520–530
7 Cleutjens, J. P., Kandala, J. C., Guarda, E., Guntaka, R. V. and Weber, K. T. (1995) Regulation of collagen degradation in the rat myocardium after infarction. J. Mol. Cell. Cardiol. 27, 1281–1292
8 Rohde, L. E., Ducharme, A., Arroyo, L. H. et al. (1999) Matrix metalloproteinase inhibition attenuates early left ventricular enlargement after experimental myocardial infarction in mice. Circulation 99, 3063–3070
9 Heymans, S., Luttun, A., Nuyens, D. et al. (1999) Inhibition of plasminogen activators or matrix metalloproteinases prevents cardiac rupture but impairs therapeutic angiogenesis and causes cardiac failure. Nat. Med. 5, 1135–1142
10 Ducharme, A., Frantz, S., Aikawa, M. et al. (2000) Targeted deletion of matrix metalloproteinase-9 attenuates left ventricular enlargement and collagen accumulation after experimental myocardial infarction. J. Clin. Invest. 106, 55–62
11 Nahrendorf, M., Hu, K., Hiller, K. H. et al. (2002) Impact of hydroxymethylglutaryl coenzyme a reductase inhibition on left ventricular remodeling after myocardial infarction: an experimental serial cardiac magnetic resonance imaging study. J. Am. Coll. Cardiol. 40, 1695–1700
12 Hayashidani, S., Tsutsui, H., Shiomi, T. et al. (2002) Fluvastatin, a 3-hydroxy-3-methylglutaryl coenzyme a reductase inhibitor, attenuates left ventricular remodeling and failure after experimental myocardial infarction. Circulation 105, 868–873
13 Nagaya, N., Nishikimi, T., Goto, Y. et al. (1998) Plasma brain natriuretic peptide is a biochemical marker for the prediction of progressive ventricular remodeling after acute myocardial infarction. Am. Heart J. 135, 21–28
14 Yasuda, S., Goto, Y., Baba, T. et al. (2000) Enhanced secretion of cardiac hepatocyte growth factor from an infarct region is associated with less severe ventricular enlargement and improved cardiac function. J. Am. Coll. Cardiol. 36, 115–121
14a Nakamura, H., Arakawa, K., Itakura, H. et al. (2006) Primary prevention of cardiovascular disease with pravastatin in Japan (MEGA study): a prospective randomised control trial. Lancet 368, 1155–1163
15 Fujimoto, N. and Iwata, K. (2001) Use of EIA to measure MMPs and TIMPs. Methods Mol. Biol. 151, 347–358
16 Yasuda, S., Goto, Y., Sumida, H. et al. (1999) Angiotensin-converting enzyme inhibition restores hepatocyte growth factor production in patients with congestive heart failure. Hypertension 33, 1374–1378
17 Squire, I. B., Evans, J., Ng, L. L., Loftus, I. M. and Thompson, M. M. (2004) Plasma MMP-9 and MMP-2 following acute myocardial infarction in man: correlation with echocardiographic and neurohumoral parameters of left ventricular dysfunction. J. Card. Failure 10, 328–333

18 Matsunaga, T., Abe, N., Kameda, K. et al. (2005) Circulating level of gelatinase activity predicts ventricular remodeling in patients with acute myocardial infarction. Int. J. Cardiol. 105, 203–208
19 Nakaya, R., Uzui, H., Shimizu, H. et al. (2005) Pravastatin suppresses the increase in matrix metalloproteinase-2 levels after acute myocardial infarction. Int. J. Cardiol. 105, 67–73
20 Wagner, D. R., Delagardelle, C., Ernens, I., Rouy, D., Vaillant, M. and Beissel, J. (2006) Matrix metalloproteinase-9 is a marker of heart failure after acute myocardial infarction. J. Card. Failure 12, 66–72
21 Higo, S., Uematsu, M., Yamagishi, M. et al. (2005) Elevation of plasma matrix metalloproteinase-9 in the culprit coronary artery in patients with acute myocardial infarction: clinical evidence from distal protection. Circ. J. 69, 1180–1185
22 Kai, H., Ikeda, H., Yasukawa, H. et al. (1998) Peripheral blood levels of matrix metalloproteases-2 and -9 are elevated in patients with acute coronary syndromes. J. Am. Coll. Cardiol. 32, 368–372
23 Fukuda, D., Shimada, K., Tanaka, A. et al. (2006) Comparison of levels of serum matrix metalloproteinase-9 in patients with acute myocardial infarction versus unstable angina pectoris versus stable angina pectoris. Am. J. Cardiol. 97, 175–180
24 Kawakami, R., Saito, Y., Kishimoto, I. et al. (2004) Overexpression of brain natriuretic peptide facilitates neutrophil infiltration and cardiac matrix metalloproteinase-9 expression after acute myocardial infarction. Circulation 110, 3306–3312
25 Davignon, J. (2004) Beneficial cardiovascular pleiotropic effects of statins. Circulation 109, III39–III43
26 El Messal, M., Beaudeux, J. L., Drissi, A. et al. (2005) Elevated serum levels of proinflammatory cytokines and biomarkers of matrix remodeling in never-treated patients with familial hypercholesterolemia. Clin. Chim. Acta 366, 185–189
27 Bader, M. (2002) Role of the local renin-angiotensin system in cardiac damage: a minireview focusing on transgenic animal models. J. Mol. Cell. Cardiol. 34, 1455–1462
28 Dechend, R., Fiebler, A., Lindschau, C. et al. (2001) Modulating angiotensin II-induced inflammation by HMG Co-A reductase inhibition. Am. J. Hypertens. 14, 55S–61S
29 Luo, J. D., Zhang, W. W., Zhang, G. P., Guan, J. X. and Chen, X. (1999) Simvastatin inhibits cardiac hypertrophy and angiotensin-converting enzyme activity in rats with aortic stenosis. Clin. Exp. Pharmacol. Physiol. 26, 903–908

Received 10 May 2006/24 August 2006; accepted 29 August 2006
Published as Immediate Publication 29 August 2006, doi:10.1042/CS20060110

Acta Crystallographica Section F
Structural Biology and Crystallization Communications
ISSN 1744-3091

Crystallization and preliminary X-ray crystallographic analysis of two vascular apoptosis-inducing proteins (VAPs) from *Crotalus atrox* venom

Tomoko Igarashi,[a] Yuko Oishi,[a] Satohiko Araki,[b] Hidezo Mori[a] and Soichi Takeda[a,c]*

[a]Department of Cardiac Physiology, National Cardiovascular Center Research Institute, 5-7-1 Fujishiro-dai, Suita, Osaka 565-8565, Japan, [b]Sugashima Marine Biological Laboratory, Graduate School of Science, Nagoya University, Toba, Mie 517-0004, Japan, and [c]Laboratory for Structural Biochemistry, Riken Harima Institute at SPring-8, 1-1-1 Kouto, Mikazuki, Sayo, Hyogo 679-5148, Japan

Correspondence e-mail: stakeda@ri.ncvc.go.jp

Received 11 May 2006
Accepted 12 June 2006

VAPs are haemorrhagic snake-venom toxins belonging to the reprolysin family of zinc metalloproteinases. *In vitro*, VAPs induce apoptosis specifically in cultured vascular endothelial cells. VAPs have a modular structure that bears structural homology to mammalian ADAMs (a disintegrin and metalloproteinases). VAP1 is a homodimer with a MW of 110 kDa in which the monomers are connected by a single disulfide bridge. VAP2 is homologous to VAP1 and exists as a monomer with a MW of 55 kDa. In the current study, several crystal forms of VAP1 and VAP2 were obtained using the vapour-diffusion method and diffraction data sets were collected using SPring-8 beamlines. The best crystals of VAP1 and VAP2 generated data sets to 2.5 and 2.15 Å resolution, respectively.

1. Introduction

Haemorrhagic snake venoms contain factors that induce apoptosis specifically in cultured vascular endothelial cells (Araki *et al.*, 1993). The vascular apoptosis-inducing proteins VAP1 and VAP2 were originally isolated from the venom of the western diamondback rattlesnake *Crotalus atrox* (Masuda *et al.*, 1997, 1998) and similar apoptotic toxins (VAPs) have been isolated from other snake venoms (Masuda *et al.*, 2001; You *et al.*, 2003; Trummal *et al.*, 2005). VAP1 is a disulfide-bonded homodimeric protein with a molecular weight of 110 kDa and an isoelectric point of 8.5. VAP2 is an acidic single-chain protein with a molecular weight of 55 kDa and an isoelectric point of 4.5 (Masuda *et al.*, 1997, 1998). VAP1 (Masuda *et al.*, 2000) and VAP2 (S. Masuda, H. Hayashi & S. Araki, in preparation) are modular metalloproteinases with nucleotide-sequence homology to genes encoding the mammalian membrane-anchored metalloproteinases known as ADAMs. ADAMs are an emerging class of metalloproteinases whose function has been implicated in cell–cell and cell–matrix adhesion and signalling. They also appear to be associated with numerous diseases including arthritis, Alzheimer's disease and cancer (White, 2003; Blobel, 2005; Seals & Courtneidge, 2003; Moss & Bartsch, 2004; Duffy *et al.*, 2003).

Viperidae snake venoms contain a number of metalloproteinases, the snake-venom metalloproteinases (SVMPs), that induce local and systemic haemorrhage by disrupting the wall of the blood vessels in envenomed patients (Gutierrez *et al.*, 2005). All known VAPs belong to the P-III class of SVMPs, which have been shown to be the most potent haemorrhagic toxins from snake venoms. The P-III SVMPs have a modular structure consisting of metalloproteinase (M), disintegrin (D) and cysteine-rich (C) domains (Fox & Serrano, 2005). SVMPs and ADAMs are members of the reprolysin group of zinc-dependent metalloproteinases, which together with astasins, serralysin and matrix metalloproteinases comprise the metzincin superfamily of metalloproteinases (Bode *et al.*, 1993). All these enzymes share a signature consensus zinc-binding motif, HE*XX*H*XX*G*XX*H, in their catalytic region that defines proteins of the class, as well as a methionine-containing turn that serves as a structural base for the three active histidine residues (Bode *et al.*, 1993).

The crystal structures of several SVMPs of the P-I class, which contain only an M domain, and of isolated domains of ADAMs have

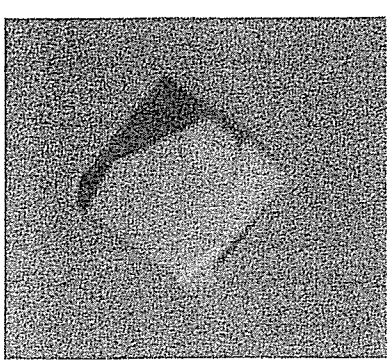

Table 1
Data-collection statistics for VAP1 crystals.

Values in parentheses are for the highest resolution shell. For each data set, a single crystal was used for measurement.

	Form 1-1	Form 1-2
Space group	$P4_12_12$	$P2_12_12_1$
Unit-cell parameters		
a (Å)	93.9	86.7
b (Å)	93.9	93.3
c (Å)	244.8	137.7
$\alpha = \beta = \gamma$ (°)	90	90
Beamline (detector)	BL45PX (Rigaku Jupiter)	BL45PX (Rigaku R-AXIS V)
Wavelength (Å)	0.98	1.0
Resolution (Å)	50–2.50 (2.59–2.50)	50–2.50 (2.59–2.50)
No. of unique reflections	38868 (3773)	38926 (3800)
R_{merge}†	0.084 (0.380)	0.072 (0.369)
$I/\sigma(I)$	18.7 (7.1)	14.4 (2.9)
Completeness (%)	99.7 (99.6)	99.4 (98.8)
Redundancy	12.7	3.91
No. of molecules in ASU	1	1
Matthews value (Å^3 Da^{-1})	2.5	2.5
Solvent content (%)	51	51

† $R_{merge} = \sum_{hkl}\sum_i |I_i(hkl) - \langle I(hkl)\rangle| / \sum_{hkl}\sum_i I_i(hkl)$, where $I_i(hkl)$ is the ith intensity measurement of reflection hkl and $\langle I(hkl)\rangle$ is its average.

been determined. However, structures of SVMPs or ADAMs containing M, D and C domains have not been determined. To understand more about the structure of P-III SVMPs and ADAMs and how it relates to the molecular mechanism of VAP-induced apoptosis, we initiated the crystallographic analysis of VAP1 and VAP2. This is the first report of the crystallization and preliminary X-ray analysis of apoptotic SVMPs. Three-dimensional crystal structures of VAP1 derived from the two distinct crystal forms described in this report have recently been described (Takeda *et al.*, 2006); the structural analysis of VAP2 is ongoing.

2. Methods

2.1. Purification

VAP1 and VAP2 were purified as described previously (Maruyama *et al.*, 2005; Masuda *et al.*, 1998) with some modifications. Briefly, crude *C. atrox* venom (Sigma–Aldrich, USA) was dissolved in buffer containing 10 m*M* Tris–HCl pH 7.0 and 10 m*M* NaCl and then applied onto a CM-Sepharose (Amersham Bioscience, USA) column equilibrated with the same buffer. VAP2 was eluted from the column with the above buffer, whereas VAP1 was eluted with buffer containing 10 m*M* Tris–HCl pH 7.0 and 50 m*M* NaCl.

The VAP1 was further purified on a hydroxylapatite column. The VAP1-containing CM-Sepharose fraction was first diluted with an equal amount of distilled water and then applied onto a hydroxylapatite column equilibrated with 25 m*M* sodium phosphate pH 7.0. VAP1 was eluted using buffer containing 50 m*M* sodium phosphate pH 7.0 and then concentrated using an Amicon Ultra membrane (Millipore) with a nominal molecular-weight limit (NMWL) of 50 000 Da. The final protein concentration was 6.5 mg ml^{-1}. During the concentration step, the buffer was replaced with 10 m*M* Tris–HCl pH 7.0.

The VAP2-containing CM-Sepharose fraction was loaded onto a Resource Q (GM Healthcare) column equilibrated with 10 m*M* Tris–HCl pH 8.0 and 50 m*M* NaCl and then eluted with a gradient of NaCl. 55 kDa molecular-weight fractions, which were eluted at about 130 m*M* NaCl, were pooled and concentrated by Amicon Ultra with a 30 000 NMWL membrane. The final protein concentration was 3.8 mg ml^{-1} in buffer containing 10 m*M* Tris–HCl pH 8.0.

2.2. Initial crystallization screen

Initial screening for appropriate crystallization conditions for VAP1 and VAP2 was carried out using the sitting-drop vapour-diffusion method and Crystal Screen (Hampton Research, USA), with or without 63 µg ml^{-1} (almost twice the molar protein concentration) of the hydroxyamate inhibitor 3-(*N*-hydroxycarboxamide)-2-isobutyl-propanoyl-Trp-methylamide (GM6001, Calbiochem) in the protein solution. A volume of 0.3–0.5 µl protein solution was mixed with an equal amount of reservoir solution and droplets were allowed to equilibrate against 0.1 ml reservoir solution at 293 K.

2.3. Diffraction data collection

Crystals were cryoprotected, mounted in a nylon loop (Hampton Research, USA) or in a Lytho Loop (Protein Wave Corp., Japan) and immediately exposed to a stream of nitrogen gas at 100 K to flash-freeze the samples. The preliminary X-ray data were collected using an in-house X-ray diffractometer (Rigaku Micromax-007 X-ray generator with R-AXIS VII imaging-plate detector) and crystals that diffracted well were selected for data acquisition using the beamlines at SPring-8. All diffraction data sets were collected using undulator beamlines (BL41XU, BL45XU) at 100 K and diffraction images were processed using the *HKL*2000 software (Otwinowski & Minor, 1997).

3. Results

3.1. VAP1 crystals

3.1.1. Crystallization. VAP1 was reproducibly crystallized in two distinct crystal forms. Crystals were initially obtained using Crystal

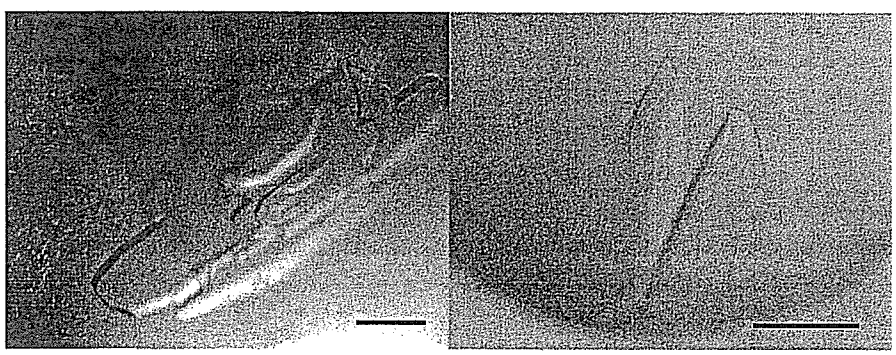

(*a*) (*b*)

Figure 1
VAP1 crystals. (*a*) Form 1-1. (*b*) Form 1-2. The scale bars indicate 0.1 mm.

Table 2
Data-collection statistics for VAP2 crystals.

Values in parentheses are for the highest resolution shell. For each data set, a single crystal was used for measurement.

	Form 2-1	Form 2-2	Form 2-3	Form 2-4	Form 2-5
GM6001	+	+	+	+	−
Space group	$P2_1$	$P2_12_12_1$	$P4_1$	$P6_322$	$C2$
Unit-cell parameters					
a (Å)	56.9	57.7	60.7	156.8	220.7
b (Å)	138.0	118.2	60.7	156.8	79.5
c (Å)	59.2	138.5	257.9	95.6	58.7
α (°)	90	90	90	90	90
β (°)	91.5	90	90	90	91.7
γ (°)	90	90	90	120	90
Beamline (detector)	BL41XU (ADSC Quantum 310R CCD detector)				
Wavelength (Å)	1.0	1.0	1.0	1.0	1.0
Resolution (Å)	50–2.15 (2.23–2.15)	50–2.50 (2.59–2.50)	50–3.20 (3.31–3.2)	50–3.80 (3.94–3.80)	50–2.70 (2.80–2.70)
No. of unique reflections	48664 (4428)	33288 (2925)	15097 (1437)	7169 (682)	26911 (2313)
R_{merge}†	0.081 (0.196)	0.089 (0.321)	0.091 (0.360)	0.117 (0.397)	0.085 (0.231)
$I/\sigma(I)$	9.8 (4.6)	10.3 (3.7)	10.9 (4.0)	8.4 (6.5)	10.1 (5.5)
Completeness (%)	98.1 (89.5)	98.6 (88.4)	99.5 (95.7)	99.8 (99.9)	95.9 (82.5)
Redundancy	3.3	6.5	7.0	19.2	3.4
No. of molecules in ASU	2	2	2	1	2
Matthews value (Å^3 Da^{-1})	2.4	2.4	2.5	3.1	2.7
Solvent content (%)	49	49	50	60	54

† $R_{merge} = \sum_{hkl}\sum_i |I_i(hkl) - \langle I(hkl)\rangle| / \sum_{hkl}\sum_i I_i(hkl)$, where $I_i(hkl)$ is the ith intensity measurement of reflection hkl and $\langle I(hkl)\rangle$ is its average.

Screen solution No. 46, but these crystals diffracted poorly. Subsequently, droplets were prepared by mixing 1 µl protein solution and 1 µl reservoir solution containing 15% PEG 8000, 0.1 *M* sodium cacodylate pH 6.5 and then equilibrated against 1 ml reservoir solution. Within a couple of weeks, using the hanging-drop method, improved tetragonal crystals (form 1-1; Fig. 1*a*) were obtained.

Orthorhombic crystals (form 1-2; Fig. 1*b*) were obtained using Additive Screen (Hampton Research, USA). The droplet was made by mixing 0.3 µl protein solution and 0.3 µl reservoir solution supplemented with one-fifth of the volume of 0.1 *M* cobalt(II) chloride (Additive Screen solution No. 4). The best crystals were obtained using the sitting-drop method after equilibration for 3 d against 0.1 ml of the same reservoir solution used to obtain form 1-1 crystals.

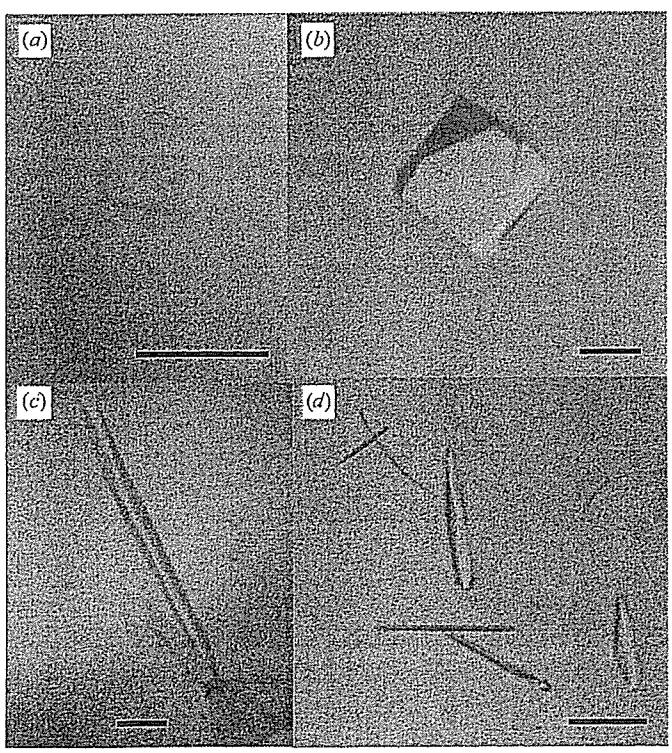

Figure 2
VAP2 crystals. (*a*) Form 2-2, (*b*) form 2-3, (*c*) form 2-4 and (*d*) form 2-5 crystals. The scale bars indicate 0.1 mm.

3.1.2. X-ray analysis. For X-ray measurements, crystals of either crystal form were soaked in a solution containing 15% PEG 8000, 5% methanol, 20% xylitol and 0.1 *M* sodium cacodylate pH 6.5 for cryoprotection prior to flash-freezing. X-ray diffraction data were obtained by the oscillation method using beamline BL45XU and an oscillation angle of 0.75° per image. Data sets were collected using a CCD detector (Rigaku Jupiter) for crystal form 1-1 or an imaging-plate detector (Rigaku R-AXIS V) for crystal form 1-2. The unit-cell parameters and the data statistics for the two crystal forms are summarized in Table 1. The structures were determined at 2.5 Å resolution by the molecular-replacement method using the P-I SVMP acutolysin-C (PDB code 1qua) as a starting model (Takeda *et al.*, 2006). The coordinates and the structure factors have been deposited in the PDB (2erq for form 1-1 and 2ero for form 1-2 crystals).

3.2. VAP2 crystals

3.2.1. Crystallization. Five distinct crystal forms of VAP2 were analyzed by X-ray diffraction. The initial screening for VAP2 crystals was performed in the presence and absence of the inhibitor GM6001.

In the presence of GM6001, Crystal Screen solution No. 10 yielded crystals. With this as a starting condition, the pH of the mother liquor, the PEG concentration and molecular weight and the species and concentrations of salts and additives were optimized and four distinct crystal forms were obtained (forms 2-1, 2-2, 2-3 and 2-4). These four forms were only obtained in the presence of GM6001 and were never obtained in its absence. Monoclinic (form 2-1) and orthorhombic (form 2-2; Fig. 2*a*) forms were obtained by the sitting-drop method under identical conditions as follows: droplets were made by mixing 0.5 µl protein solution with 0.5 µl reservoir solution containing 30% PEG 8000, 0.1 *M* ammonium acetate, 0.1 *M* sodium cacodylate pH 6.5 and were equilibrated against 0.1 ml reservoir solution. Tetragonal form crystals (form 2-3; Fig. 2*b*) were obtained by adding a one-tenth volume of 1 *M* potassium chloride (Additive Screen solution No. 16)

to the mother liquor and using a reservoir solution containing 30% PEG 8000, 0.1 *M* ammonium acetate, 0.1 *M* sodium acetate pH 4.6 with the same drop and reservoir volumes described above. Hexagonal crystals (form 2-4; Fig. 2*c*) were obtained by the hanging-drop method using 1 ml of a reservoir solution containing 20% PEG 20 000, 0.2 *M* calcium acetate, 0.1 *M* sodium cacodylate pH 6.5. The droplet was made by mixing 1 µl protein solution and 1 µl reservoir solution supplemented with a one-fifth volume of 0.3 *M* glycyl-glycyl-glycine solution (Additive Screen solution No. 34).

In the absence of GM6001, crystals were obtained with Crystal Screen solution No. 46, but these crystals yielded poor diffraction data. To improve the quality of the crystals, several additives were screened. Monoclinic crystals (form 2-5; Fig. 2*d*) were obtained by adding a one-tenth volume of 40% *n*-propanol solution (Additive Screen solution No. 90) to the reservoir solution (final composition 4% *n*-propanol, 16.2% PEG 8000, 0.18 *M* calcium acetate, 0.09 *M* sodium cacodylate pH 6.5). A mixture of 0.5 µl protein solution and 0.5 µl reservoir solution was equilibrated against 0.1 ml reservoir solution. These form 2-5 crystals were only obtained in the absence of GM6001 and were never obtained in its presence.

3.2.2. X-ray analysis. The mother liquors of the form 2-2 and 2-3 crystals were suitable for freezing; all others were first cryoprotected. For form 2-1 and 2-4 crystals, 20% glycerol was added to the reservoir solution for cryoprotection. For form 2-1, the cryogenic solution was added gradually to the crystal droplet in order to avoid cracking induced by osmotic shock. Crystal form 2-5 was rinsed in a solution containing 15% PEG 8000, 5% methanol, 20% xylitol and 0.1 *M* sodium cacodylate pH 6.5 and then immediately flash-frozen at 100 K. Because these crystals were extremely thin and fragile, they were mounted in a LithoLoop, an etched Mylar film, to prevent bending of the crystal.

All diffraction data sets for the VAP2 crystals were acquired using the oscillation method and beamline BL41XU (the oscillation angle was 1.0° for all data sets) at a wavelength of 1.0 Å and data were collected using an ADSC Quantum 310R detector. The unit-cell parameters and statistics for the data sets are summarized in Table 2. The estimated number of molecules in the asymmetric unit for each crystal form was obtained by a preliminary molecular-replacement method using *MOLREP* from the *CCP*4 suite (Collaborative Computational Project, Number 4, 1994) and the metalloproteinase (M) and cysteine-rich (C) domains of VAP1 (Takeda *et al.*, 2006) as the starting models. Structural analyses of these crystals along with the molecular-replacement phases are ongoing.

We thank Mariko Tomisako for her help in crystallization experiments and the staff of SPring-8 for assistance with data acquisition. This work was partly supported by Grant Nano-001 for Research on Advanced Medical Technology from the Ministry of Health, Labour and Welfare of Japan and by grants from the Takeda Science Foundation, from the Kao Foundation for Arts and Science and from the Senri Life Science Foundation.

References

Araki, S., Ishida, T., Yamamoto, T., Kaji, K. & Hayashi, H. (1993). *Biochem. Biophys. Res. Commun.* **190**, 148–153.
Blobel, C. P. (2005). *Nature Rev. Mol. Cell Biol.* **6**, 32–43.
Bode, W., Gomis-Ruth, F. X. & Stockler, W. (1993). *FEBS Lett.* **331**, 134–140.
Collaborative Computational Project, Number 4 (1994). *Acta Cryst.* D**50**, 760–763.
Duffy, M. J., Lynn, D. J., Lloyd, A. T. & O'Shea, C. M. (2003). *Thromb. Haemost.* **89**, 622–631.
Fox, J. W. & Serrano, S. M. (2005). *Toxicon*, **45**, 969–985.
Gutierrez, J. M., Rucavado, A., Escalante, T. & Diaz, C. (2005). *Toxicon*, **45**, 997–1011.
Maruyama, J., Hayashi, H., Miao, J., Sawada, H. & Araki, S. (2005). *Toxicon*, **46**, 1–6.
Masuda, S., Araki, S., Yamamoto, T., Kaji, K. & Hayashi, H. (1997). *Biochem. Biophys. Res. Commun.* **235**, 59–63.
Masuda, S., Hayashi, H. & Araki, S. (1998). *Eur. J. Biochem.* **253**, 36–41.
Masuda, S., Hayashi, H., Atoda, H., Morita, T. & Araki, S. (2001). *Eur. J. Biochem.* **268**, 3339–3345.
Masuda, S., Ohta, T., Kaji, K., Fox, J. W., Hayashi, H. & Araki, S. (2000). *Biochem. Biophys. Res. Commun.* **278**, 197–204.
Moss, M. L. & Bartsch, J. W. (2004). *Biochemistry*, **43**, 7227–7235.
Otwinowski, Z. & Minor, W. (1997). *Methods Enzymol.* **276**, 307–326.
Seals, D. F. & Courtneidge, S. A. (2003). *Genes Dev.* **17**, 7–30.
Takeda, S., Igarashi, T., Mori, H. & Araki, S. (2006). *EMBO J.* **25**, 2388–2396.
Trummal, K., Tonismagi, K., Siigur, E., Aaspollu, A., Lopp, A., Sillat, T., Saat, R., Kasak, L., Tammiste, I., Kogerman, P., Kalkkinen, N. & Siigur, J. (2005). *Toxicon*, **46**, 46–61.
White, J. M. (2003). *Curr. Opin. Cell Biol.* **15**, 598–606.
You, W. K., Seo, H. J., Chung, K. H. & Kim, D. S. (2003). *J. Biochem. (Tokyo)*, **134**, 739–749.

Available online at www.sciencedirect.com
ScienceDirect
Radiation Physics and Chemistry 75 (2006) 1841–1849
Radiation Physics and Chemistry
www.elsevier.com/locate/radphyschem

K-edge angiography utilizing a tungsten plasma X-ray generator in conjunction with gadolinium-based contrast media

Eiichi Sato[a,*], Yasuomi Hayasi[a], Etsuro Tanaka[b], Hidezo Mori[c], Toshiaki Kawai[d], Takashi Inoue[e], Akira Ogawa[e], Shigehiro Sato[f], Kazuyoshi Takayama[g], Jun Onagawa[h], Hideaki Ido[h]

[a]*Department of Physics, Iwate Medical University, 3-16-1 Honchodori, Morioka 020-0015, Japan*
[b]*Department of Nutritional Science, Faculty of Applied Bio-science, Tokyo University of Agriculture, 1-1-1 Sakuragaoka, Setagaya-ku 156-8502, Japan*
[c]*Department of Cardiac Physiology, National Cardiovascular Center Research Institute, 5-7-1 Fujishirodai, Suita, Osaka 565-8565, Japan*
[d]*Electron Tube Division #2, Hamamatsu Photonics K. K., 314-5 Shimokanzo, Iwata 438-0193, Japan*
[e]*Department of Neurosurgery, School of Medicine, Iwate Medical Universichimaru, Morioka 020-8505, Japan*
[f]*Department of Microbiology, School of Medicine, Iwate Medical University, 19-1 Uchimaru, Morioka 020-8505, Japan*
[g]*Shock Wave Research Center, Institute of Fluid Science, Tohoku University, 2-1-1 Katahira, Sendai 980-8577, Japan*
[h]*Department of Applied Physics and Informatics, Faculty of Engineering, Tohoku Gakuin University, 1-13-1 Chuo, Tagajo 985-8537, Japan*

Accepted 23 November 2005

Abstract

The tungsten plasma flash X-ray generator is useful in order to perform high-speed enhanced K-edge angiography using cone beams because K-series characteristic X-rays from the tungsten target are absorbed effectively by gadolinium-based contrast media. In the flash X-ray generator, a 150 nF condenser is charged up to 80 kV by a power supply, and flash X-rays are produced by the discharging. The X-ray tube is a demountable diode, and the turbomolecular pump evacuates air from the tube with a pressure of approximately 1 mPa. Since the electric circuit of the high-voltage pulse generator employs a cable transmission line, the high-voltage pulse generator produces twice the potential of the condenser charging voltage. At a charging voltage of 80 kV, the estimated maximum tube voltage and current were approximately 160 kV and 40 kA, respectively. When the charging voltage was increased, the characteristic X-ray intensities of tungsten K_α lines increased. The K_α lines were clean, and hardly any bremsstrahlung rays were detected. The X-ray pulse widths were approximately 110 ns, and the time-integrated X-ray intensity had a value of approximately 0.35 mGy at 1.0 m from the X-ray source with a charging voltage of 80 kV. Angiography was performed

*Corresponding author.
E-mail address: dresato@iwate-med.ac.jp (E. Sato).

0969-806X/$ - see front matter
doi:10.1016/j.radphyschem.2005.11.015

using a film-less computed radiography (CR) system and gadolinium-based contrast media. In angiography of non-living animals, we observed fine blood vessels of approximately 100 μm with high contrasts.

PACS: 52.59.Mv; 52.80.Vp; 87.59.Dj; 87.64.Gb

Keywords: Angiography; Gadolinium-based contrast media; Characteristic X-rays; Quasi-monochromatic X-rays; Tungsten K_α lines

1. Introduction

The successful uses of monochromatic parallel beams from synchrotron orbital radiation in recent years have greatly increased the demand for phase-contrast radiography (Davis et al., 1995; Momose et al., 1996; Ando et al., 2002) and enhanced K-edge angiography (Thompson et al., 1992; Mori et al., 1996; Hyodo et al., 1998). In particular, the parallel beams with photon energies of approximately 35 keV have been employed to perform angiography, because the beams are absorbed effectively by iodine-based contrast media with a K-absorption edge of 33.2 keV. Without using a synchrotron, we have developed an X-ray generator utilizing a cerium-target tube, and have performed cone-beam K-edge angiography achieved with cerium K_α rays of 34.6 keV (Sato et al., 2004a, b, c).

Gadolinium-based contrast media with a K-edge of 50.2 keV have been employed to perform magnetic resonance angiography (MRA), and the gadolinium density has been increasing. In view of this situation, ytterbium K_α rays (52.0 keV) are useful for enhanced K-edge angiography, because the K_α rays are absorbed effectively by gadolinium media. As compared with angiography using iodine media, the absorbed dose can be decreased considerably utilizing angiography achieved with gadolinium media. However, because ytterbium is a lanthanide series element and tends to oxidize in the atmosphere, K_α rays of tantalum (57.1 keV) and tungsten (58.9 keV) are also useful to perform angiography.

To produce high-dose-rate X-rays, several different flash X-ray generators have been developed (Sato et al., 1990, 1994a, b; Shikoda et al., 1994; Takahashi et al., 1994), and plasma flash X-ray generators (Sato et al., 2003a, b, 2004a, b, c, 2005a, b, c) have been developed to perform a preliminary experiment for producing hard X-ray lasers. In the plasma, the bremsstrahlung X-rays are absorbed effectively and are converted into fluorescent rays, and intense and clean K-series characteristic X-rays of nickel and copper have been produced from the axial direction of weakly ionized linear plasma. However, it is difficult to increase the photon energies of characteristic X-rays because the plasma transmits high-photon-energy bremsstrahlung X-rays. In view of this situation, we have developed a compact flash X-ray generator (Sato et al., 2004a, b, c, 2005a, b, c) and have succeeded in producing clean high-photon-energy characteristic X-rays utilizing the angle dependence of bremsstrahlung X-rays, because bremsstrahlung rays are not emitted in the opposite direction to that of electron trajectory in Sommerfeld's theory.

In this article, we describe an intense quasi-monochromatic plasma flash X-ray generator with a tungsten target tube, and used it to perform a preliminary study on angiography achieved with tungsten K_α rays.

2. Principle of K-edge angiography

Fig. 1 shows the mass attenuation coefficients of gadolinium at the selected energies; the coefficient curve is discontinuous at the gadolinium K-edge. The average photon energy of the tungsten K_α lines is shown above the gadolinium K-edge. The average photon energy is 58.9 keV, and gadolinium contrast media with a K-absorption edge of 50.2 keV absorb the lines easily. Therefore, blood vessels were observed with high contrasts.

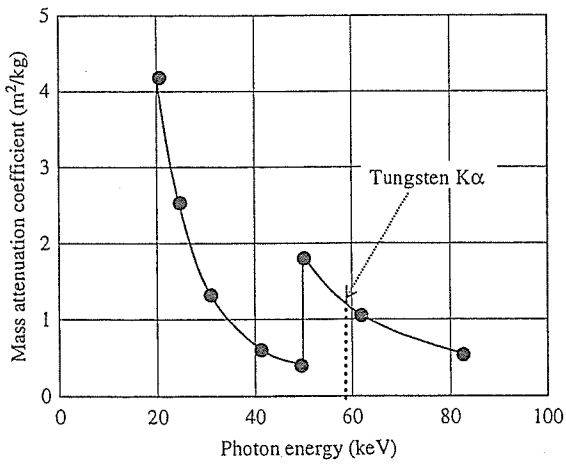

Fig. 1. Mass attenuation coefficients of gadolinium. The average photon energy of tungsten K_α lines is shown above gadolinium K edge.

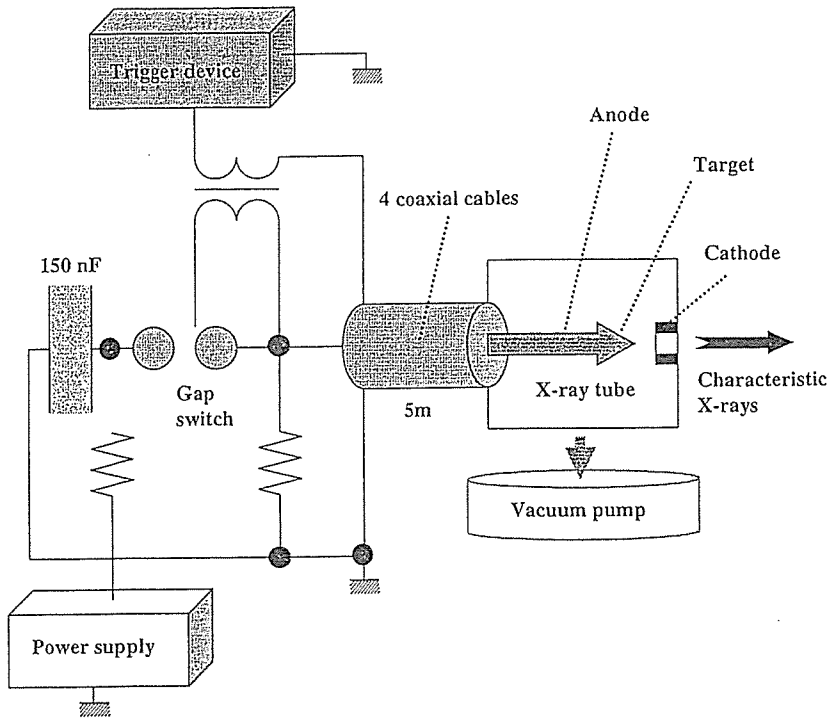

Fig. 2. Block diagram including the high-voltage circuit of the intense quasi-monochromatic plasma flash X-ray generator with a tungsten-target tube.

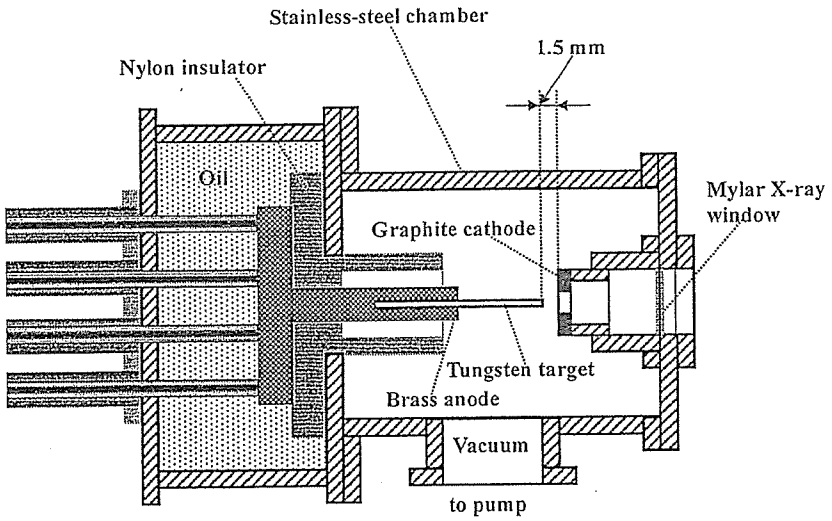

Fig. 3. Schematic drawing of a flash X-ray tube with a rod-shaped tungsten target.

3. Generator

3.1. High-voltage circuit

Fig. 2 shows a block diagram of a high-intensity plasma flash X-ray generator. The generator consists of the following essential components: a high-voltage power supply, a high-voltage condenser with a capacity of approximately 150 nF, an air gap switch, a turbomolecular pump, a thyratron pulse generator as a trigger device and a flash X-ray tube. In this generator, a coaxial cable transmission line is employed in order to

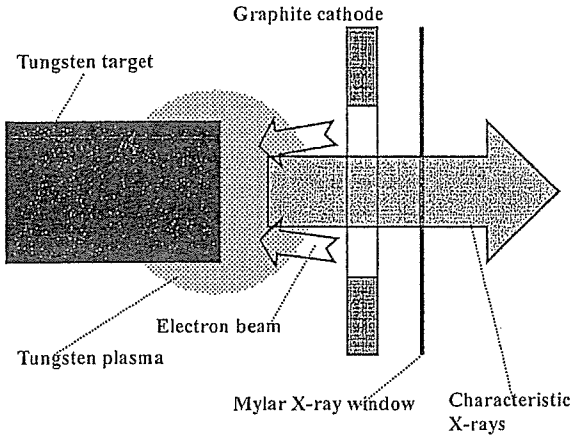

Fig. 4. Irradiation of K-series characteristic X-rays of tungsten.

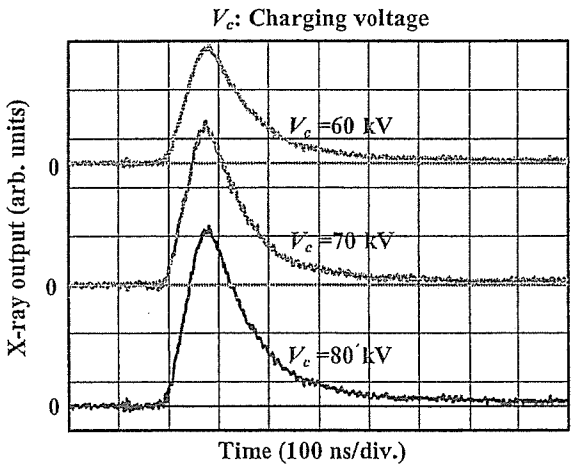

Fig. 5. X-ray outputs detected using a combination of a plastic scintillator and a photomultiplier.

increase maximum tube voltage using high-voltage reflection. The high-voltage main condenser is charged up to 80 kV by the power supply, and electric charges in the condenser are discharged to the tube through the four cables after closing the gap switch with the trigger device.

3.2. X-ray tube

The X-ray tube is a demountable cold-cathode diode that is connected to the turbomolecular pump with a pressure of approximately 1 mPa (Fig. 3). This tube consists of the following major parts: a ring-shaped graphite cathode with an inside diameter of 4.5 mm, a stainless-steel vacuum chamber, a nylon insulator, a polyethylene terephthalate (Mylar) X-ray window 0.25 mm in thickness and a rod-shaped tungsten target 3.0 mm in diameter. The distance between the target and cathode electrodes can be regulated from the outside of the tube, and is set to 1.5 mm. As electron beams from the cathode electrode are roughly converged to the target by the electric field in the tube, evaporation leads to the formation of weakly ionized plasma, consisting of tungsten ions and electrons, around the target. Because bremsstrahlung rays are not emitted in the opposite direction to that of electron trajectory (Fig. 4), tungsten K-series characteristic X-rays can be produced without using a filter.

4. Characteristics

4.1. Tube voltage and current

In this generator, it was difficult to measure the tube voltage and current since the tube voltages were high, and there was no space to set a current transformer for measuring the tube current. Currently, the voltage and

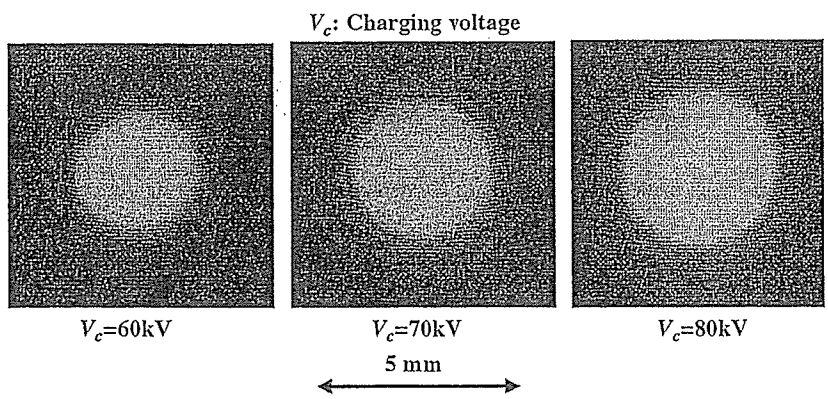

Fig. 6. Images of characteristic X-ray source obtained using a pinhole camera with changes in the charging voltage.

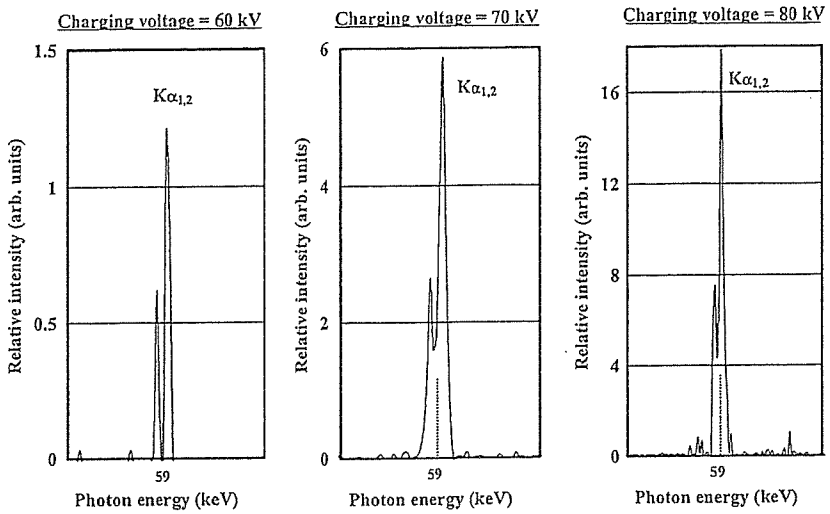

Fig. 7. X-ray spectra from a tungsten target. The spectra were measured using a transmission type spectrometer with a lithium fluoride curved crystal.

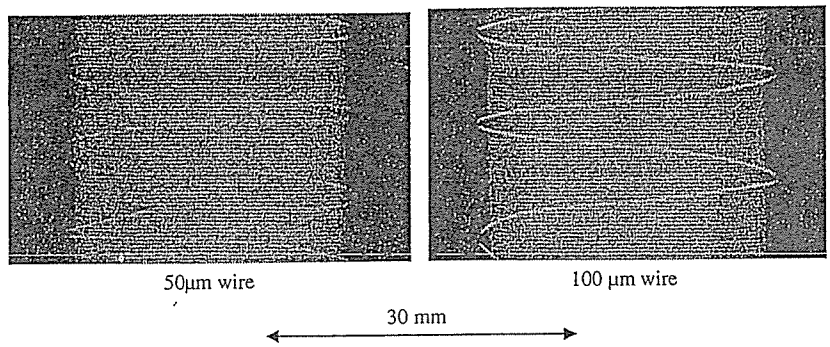

Fig. 8. Radiograms of tungsten wires coiled around rods made of polymethyl methacrylate.

current roughly display damped oscillations. When the charging voltage was increased, both the maximum tube voltage and current increased. At a charging voltage of 80 kV, the estimated maximum values of the tube voltage and current were approximately 160 kV (two times the charging voltage) and 40 kA, respectively.

4.2. X-ray output

X-ray output pulse was detected using a combination of a plastic scintillator and a photomultiplier (Fig. 5). The X-ray pulse height substantially increased with corresponding increases in the charging voltage. The X-ray pulse widths were approximately 110 ns, and the time-integrated X-ray intensity measured by a thermoluminescence dosimeter (Kyokko TLD Reader 1500 having MSO-S elements without energy compensation) had a value of approximately 0.35 mGy at 1.0 m from the X-ray source with a charging voltage of 80 kV.

4.3. X-ray source

In order to observe the plasma X-ray source, we employed a 100-μm-diameter pinhole camera and an X-ray film (Polaroid XR-7) (Fig. 6). When the charging voltage was increased, the plasma X-ray source grew, and both spot dimension and intensity increased. Because the X-ray intensity is the highest at the center of the spot, both the dimension and intensity decreased according to both increases in the thickness of a filter for absorbing X-rays and decreases in the pinhole diameter.

4.4. X-ray spectra

X-ray spectra were measured using a transmission-type spectrometer with a lithium fluoride curved crystal 0.5 mm in thickness. The X-ray intensities of the spectra were detected by an imaging plate of a computed radiography (CR) system (Sato et al., 2000) (Konica Minolta Regius 150) with a wide dynamic range, and

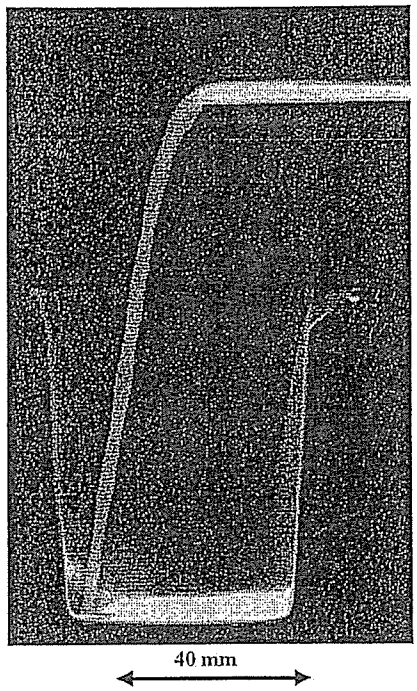

Fig. 9. Radiogram of water falling into polypropylene beaker from a glass test tube.

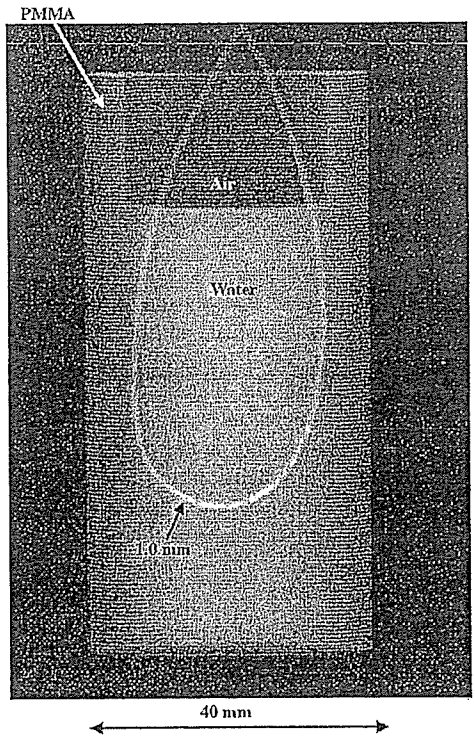

Fig. 10. Angiography of a Teflon tube using a contrast medium which contains approximately 65% gadodiamidehydrate.

Fig. 11. Angiography of a rabbit ear using gadolinium oxide powder.

relative X-ray intensity was calculated from Dicom original digital data corresponding to X-ray intensity; the data was scanned by Dicom viewer in the film-less CR system. Subsequently, the relative X-ray intensity as a function of the data was calibrated using a conventional X-ray generator, and we confirmed that the intensity was proportional to the exposure time. Fig. 7 shows measured spectra from the tungsten target. We observed clean K_α lines, while bremsstrahlung rays were hardly detected. The K_α intensity substantially increased with increases in the charging voltage.

5. Angiography

The flash angiography was performed by the CR system at 1.2 m from the X-ray source, and the charging voltage was 80 kV.

Firstly, rough measurements of spatial resolution were made using wires. Fig. 8 shows radiograms of tungsten wires coiled around rods made of polymethyl methacrylate (PMMA). Although the image contrast decreased somewhat with decreases in the wire diameter, due to blurring of the image caused by the sampling pitch of 87.5 μm, a 50-μm-diameter wire could be observed.

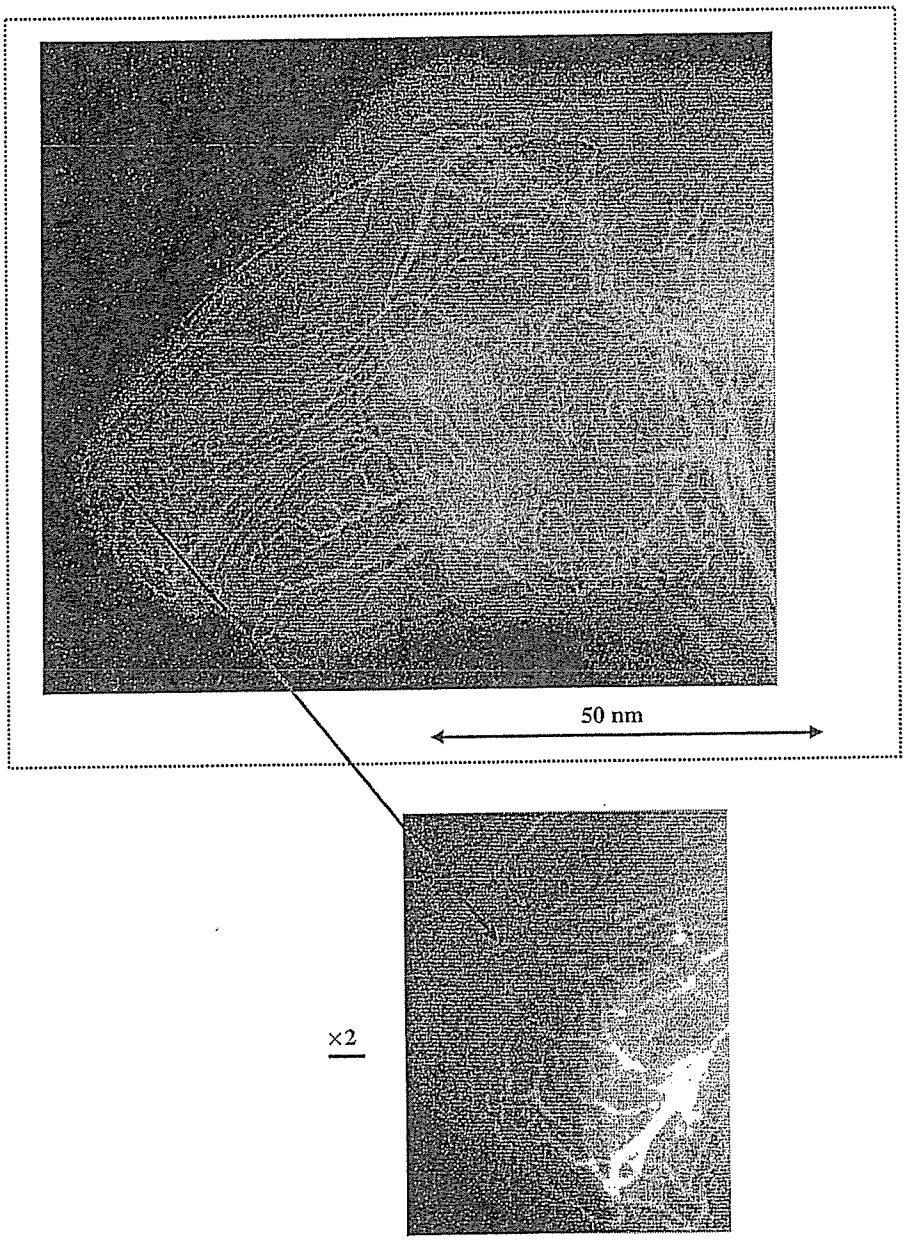

Fig. 12. Angiography of a rabbit head using gadolinium oxide powder.

The image of water (20% gadolinium oxide suspension) falling into a polypropylene beaker from a plastic test tube is shown in Fig. 9. The diameter of gadolinium oxide powder ranges from 1 to 10 μm. Because the X-ray duration was about 100 ns, the stop-motion image of water could be obtained.

Fig. 10 shows an angiogram of a polytetrafluoroethylene (Teflon) tube in a PMMA case using a contrast medium which contains approximately 65% gadodiamidehydrate, and a high-contrast tube with a bore diameter of 1.0 mm is observed. Figs. 11 and 12 show angiograms of a rabbit ear and head using gadolinium oxide powder, and fine blood vessels of approximately 100 μm were visible.

6. Conclusions and outlook

In summary, we succeeded in producing K_α rays of tungsten and in performing K-edge angiography using gadolinium contrast media with a K-edge of 50.2 keV, and this K-edge angiography could be a useful technique

to decrease the dose absorbed by patients. Although we employed tungsten K_α (58.9 keV) rays, L-series characteristic rays should be absorbed before angiography using a filter.

We obtained sufficient X-ray intensity for CR angiography with X-ray durations of approximately 100 ns, and the intensity can be increased by increasing the charging voltage at a constant target–cathode space. In an empirical equation, because the characteristic X-ray intensity is proportional to approximately 1.5th power of the voltage difference between the tube voltage and the critical excitation voltage, optimum intensity for angiography can be controlled. In this research, the generator produced instantaneous number of K photons was approximately 1×10^9 photons/cm^2 per pulse at 1.0 m from the source.

Because the dimensions of the X-ray source are primarily determined by the target diameter, the diameter should be minimized in order to improve the spatial resolution, and can be reduced to approximately 0.5 mm. Subsequently, the sampling pitch can be decreased to 43.8 μm using a CR system (Konica Minolta Regius 190) to observe fine blood vessels of approximately 50 μm diameter.

Using this flash X-ray generator, enhanced K-edge angiography using iodine contrast media can also be performed using a cerium target. In addition, steady-state monochromatic X-rays can be produced by a similar tube utilizing a hot cathode and a constant high-voltage power supply. In addition, fine focusing can be realized using tungsten or molybdenum target, and these X-ray generators could be employed to perform quasi-monochromatic phase-contrast radiography for edge enhancement.

Acknowledgments

This work was supported by Grants-in-Aid for Scientific Research (13470154, 13877114, 16591181 and 16591222) and Advanced Medical Scientific Research from MECSST, Health and Labor Sciences Research Grants (RAMT-nano-001, RHGTEFB-genome-005 and RHGTEFB-saisei-003), grants from the Keiryo Research Foundation, the Promotion and Mutual Aid Corporation for Private Schools of Japan, the Japan Science and Technology Agency (JST) and the New Energy and Industrial Technology Development Organization (NEDO, Industrial Technology Research Grant Program in 2003).

References

Ando, M., Maksimenko, M., Sugiyama, H., Pattanasiriwisawa, W., Hyodo, K., Uyama, C., 2002. A simple X-ray dark- and bright-field imaging using achromatic Laue optics. Jpn. J. Appl. Phys. 41, L1016–L1018.

Davis, T.J., Gao, D., Gureyev, T.E., Stevenson, A.W., Wilkins, S.W., 1995. Phase-contrast imaging of weakly absorbing materials using hard X-rays. Nature 373, 595–597.

Hyodo, K., Ando, M., Oku, Y., Yamamoto, S., Takeda, T., Itai, Y., Ohtsuka, S., Sugishita, Y., Tada, J., 1998. Development of a two-dimensional imaging system for clinical applications of intravenous coronary angiography using intense synchrotron radiation produced by a multipole wiggler. J. Synchrotron Rad. 5, 1123–1126.

Momose, A., Takeda, T., Itai, Y., Hirano, K., 1996. Phase-contrast X-ray computed tomography for observing biological soft tissues. Nat. Med. 2, 473–475.

Mori, H., Hyodo, K., Tanaka, E., Mohammed, M.U., Yamakawa, A., Shinozaki, Y., Nakazawa, H., Tanaka, Y., Sekka, T., Iwata, Y., Honda, S., Umetani, K., Ueki, H., Yokoyama, T., Tanioka, K., Kubota, M., Hosaka, H., Ishizawa, N., Ando, M., 1996. Small-vessel radiography in situ with monochromatic synchrotron radiation. Radiology 201, 173–177.

Sato, E., Kimura, S., Kawasaki, S., Isobe, H., Takahashi, K., Tamakawa, Y., Yanagisawa, T., 1990. Repetitive flash X-ray generator utilizing a simple diode with a new type of energy-selective function. Rev. Sci. Instrum. 61, 2343–2348.

Sato, E., Takahashi, K., Sagae, M., Kimura, S., Oizumi, T., Hayasi, Y., Tamakawa, Y., Yanagisawa, T., 1994a. Sub-kilohertz flash X-ray generator utilizing a glass-enclosed cold-cathode triode. Med. Biol. Eng. Comput. 32, 289–294.

Sato, E., Sagae, M., Takahashi, K., Shikoda, A., Oizumi, T., Hayasi, Y., Tamakawa, Y., Yanagisawa, T., 1994b. 10kHz microsecond pulsed X-ray generator utilizing a hot-cathode triode with variable durations for biomedical radiography. Med. Biol. Eng. Comput. 32, 295–301.

Sato, E., Sato, K., Tamakawa, Y., 2000. Film-less computed radiography system for high-speed imaging. Ann. Rep. Iwate Med. Univ. Sch. Lib. Arts Sci. 35, 13–23.

Sato, E., Hayasi, Y., Germer, R., Tanaka, E., Mori, H., Kawai, T., Obara, H., Ichimaru, T., Takayama, K., Ido, H., 2003a. Irradiation of intense characteristic X-rays from weakly ionized linear molybdenum plasma. Jpn. J. Med. Phys. 23, 123–131.

Sato, E., Hayasi, Y., Germer, R., Tanaka, E., Mori, H., Kawai, T., Ichimaru, T., Takayama, K., Ido, H., 2003b. Quasi-monochromatic flash X-ray generator utilizing weakly ionized linear copper plasma. Rev. Sci. Instrum. 74, 5236–5240.

Sato, E., Sagae, M., Tanaka, E., Hayasi, Y., Germer, R., Mori, H., Kawai, T., Ichimaru, T., Sato, S., Takayama, Y., Ido, H., 2004a. Quasi-monochromatic flash X-ray generator utilizing a disk-cathode molybdenum tube. Jpn. J. Appl. Phys. 43, 7324–7328.

Sato, E., Hayasi, Y., Germer, R., Tanaka, E., Mori, H., Kawai, T., Ichimaru, T., Sato, S., Takayama, K., Ido, H., 2004b. Sharp characteristic X-ray irradiation from weakly ionized linear plasma. J. Electron Spectrosc. Related Phenom. 137–140, 713–720.

Sato, E., Tanaka, E., Mori, H., Kawai, T., Ichimaru, T., Sato, S., Takayama, K., Ido, H., 2004c. Demonstration of

enhanced K-edge angiography using a cerium target X-ray generator. Med. Phys. 31, 3017–3021.

Sato, E., Tanaka, E., Mori, H., Kawai, T., Ichimaru, T., Sato, S., Takayama, Y., Ido, H., 2005a. Compact monochromatic flash X-ray generator utilizing a disk-cathode molybdenum tube. Med. Phys. 32, 49–54.

Sato, E., Tanaka, E., Mori, H., Kawai, T., Sato, S., Takayama, Y., 2005b. High-speed enhanced K-edge angiography utilizing cerium plasma X-ray generator. Opt. Eng. 44, 049001–049016.

Sato, E., Tanaka, E., Mori, H., Kawai, T., Sato, S., Takayama, Y., 2005c. Clean monochromatic X-ray irradiation from weakly ionized linear copper plasma. Opt. Eng. 44, 049002–049016.

Shikoda, A., Sato, E., Sagae, M., Oizumi, T., Tamakawa, Y., Yanagisawa, T., 1994. Repetitive flash X-ray generator having a high-durability diode driven by a two-cable-type line pulser. Rev. Sci. Instrum. 65, 850–856.

Takahashi, K., Sato, E., Sagae, M., Oizumi, T., Tamakawa, Y., Yanagisawa, T., 1994. Fundamental study on a long-duration flash X-ray generator with a surface-discharge triode. Jpn. J. Appl. Phys. 33, 4146–4151.

Thompson, A.C., Zeman, H.D., Brown, G.S., Morrison, J., Reiser, P., Padmanabahn, V., Ong, L., Green, S., Giacomini, J., Gordon, H., Rubenstein, E., 1992. First operation of the medical research facility at the NSLS for coronary angiography. Rev. Sci. Instrum. 63, 625–628.

ELSEVIER

Cardiovascular Research 72 (2006) 412–421

Cardiovascular Research

www.elsevier.com/locate/cardiores

Heavy ion radiation up-regulates Cx43 and ameliorates arrhythmogenic substrates in hearts after myocardial infarction

Mari Amino [a,f,1], Koichiro Yoshioka [a,1], Teruhisa Tanabe [a], Etsuro Tanaka [b], Hidezo Mori [c], Yoshiya Furusawa [d], Wojciech Zareba [e], Masatoshi Yamazaki [f], Harumichi Nakagawa [f], Haruo Honjo [f], Kenji Yasui [f], Kaichiro Kamiya [f], Itsuo Kodama [f,*]

[a] *Department of Cardiology, Tokai University School of Medicine, Isehara, Japan*
[b] *Department of Nutritional Sciences, Tokyo University of Agriculture, Tokyo, Japan*
[c] *Department of Cardiac Physiology, National Cardiovascular Center Research Institute, Osaka, Japan*
[d] *National Institute of Radiological Sciences, Chiba, Japan*
[e] *Cardiology Unit, University of Rochester, Rochester, USA*
[f] *Research Institute of Environmental Medicine, Nagoya University, Nagoya, Japan*

Received 4 June 2006; received in revised form 12 September 2006; accepted 15 September 2006
Available online 20 September 2006
Time for primary review 17 days

Abstract

Objective: Radiation has been shown to enhance intercellular communication in the skin and lungs through an increase of connexin43 (Cx43) expression. If analogous Cx43 up-regulation is induced in the diseased heart, it would provide a new perspective in radiation therapy for arrhythmias. The aim of the present study is to test this hypothesis.
Methods: Non-transmural myocardial infarction (MI) was created in 24 rabbits by microsphere injection into the coronary arteries. Twenty-four rabbits without MI were used as controls. Targeted external heavy ion beam irradiation (THIR; 15 Gy) was applied 2 weeks after MI with an accelerator (HIMAC, Chiba, Japan).
Results: The THIR was associated with an increase of Cx43 mRNA and protein levels in the left ventricle in control as well as in MI rabbits. THIR also increased lateralization of Cx43, which was no longer colocalized with cadherins. In MI hearts, immunoreactive Cx43 signals were reduced in the peri-infarct zone, and the reduction was reversed by THIR. *In-vivo* epicardial potential mapping on the free wall (64 unipolar electrodes to cover 7 × 7 mm) in MI hearts revealed reduced conduction velocity, whereas dispersion of the activation-recovery interval (ARI) was increased compared with controls, and these changes were reversed by THIR. The vulnerability for ventricular tachyarrhythmias (VT/VF), which was estimated by programmed stimulation, was increased in MI hearts, and this increased vulnerability to arrhythmias was reversed by THIR.
Conclusions: THIR increases Cx43 expression, improves the conductivity, decreases the spatial heterogeneity of repolarization, and reduces the vulnerability of rabbit hearts to ventricular arrhythmias after MI. THIR could have an antiarrhythmic potential through an improvement of electrical coupling.

Keywords: Gap junctions; Connexin43; Heavy ion radiaton; Myocardial infarction; Ventricular arrhythmias; Arrhythmia (mechanisms); Epicardial mapping

1. Introduction

Modalities currently available for treatment and prevention of life-threatening ventricular tachyarrhythmias (VT/VF) are antiarrhythmic drugs, catheter ablation and implantable cardioverter/defibrillator (ICD). The usefulness of these therapeutic options is limited by either low efficiency, intolerable side

* Corresponding author. Tel.: +81 52 789 3871; fax: +81 52 789 3890.
E-mail address: ikodama@riem.nagoya-u.ac.jp (I. Kodama).
[1] The first two authors contributed equally to this work.

0008-6363/$ - see front matter © 2006 European Society of Cardiology. Published by Elsevier B.V. All rights reserved.
doi:10.1016/j.cardiores.2006.09.010